remote sensing

MDPI

Article

Deriving Regional Snow Line Dynamics during the Ablation Seasons 1984–2018 in European Mountains

Zhongyang Hu [1,*], Andreas J. Dietz [1] and Claudia Kuenzer [1,2]

[1] German Remote Sensing Data Center (DFD), German Aerospace Center (DLR), Muenchener Strasse 20, D-82234 Wessling, Germany; Andreas.Dietz@dlr.de (A.J.D.); Claudia.Kuenzer@dlr.de (C.K.)
[2] Department of Remote Sensing, Institute of Geography and Geology, University of Wuerzburg, Am Hubland, D-97074 Wuerzburg, Germany
* Correspondence: Zhongyang.Hu@dlr.de; Tel.: + 49-08153-282851

Received: 8 March 2019; Accepted: 15 April 2019; Published: 17 April 2019

Abstract: Snowmelt in the mid-latitude European mountains is undergoing significant spatiotemporal changes. Regional snow line elevation (RSLE) is an appropriate indicator for assessing snow cover variations in mountain areas. To derive regional snow line dynamics during the ablation seasons 1984–2018, the present study unprecedentedly introduced a readily applicable framework. The framework constitutes four steps: atmospheric and topographic correction, snow classification, RSLE retrieval, and regional snow line retreat curve (RSLRC) derivation. The developed framework has been successfully applied to 8641 satellite images acquired by Landsat, ASTER, and Sentinel-2. The results of the intra-annual regional snow line variations show that: (1) regional snow lines in the Alpine catchments preserve the longest; (2) RSLEs are lower in the northern Pyrenees than in the southern part; (3) regional snow lines persist the shortest in the Carpathian catchments; and (4) during the end of the ablation season 2018, intermediate snowfall events in the catchments Adda, Tagliamento, and Uzh are observed. In terms of the long-term inter-annual variations, significantly accelerating snow line recession is detected in the northern Pyrenean catchment Ariege. In the Alpine catchment Alpenrhein and Drac, RSLRCs are shifting towards lower accumulated air-temperature (AT) significantly, with the magnitude of −3.77 °C·a^{-1} (Alpenrhein) and −3.99 °C·a^{-1} (Drac).

Keywords: snow line dynamics; European mountains; ablation season; regional snow line elevation (RSLE); regional snow line retreat curves (RSLRCs); M-estimation; Landsat; ASTER; Sentinel-2; time-series

1. Introduction

Snowmelt during ablation seasons is essential with regards to runoff generation, winter sports/tourism, biodiversity, and natural disasters. Due to ongoing climate change, snowmelt is undergoing significant spatiotemporal variations [1–4]. In the Northern Hemisphere, IPCC [5] projected with a high confidence that snow cover area (SCA) thereof was continuously decreasing during the ablation seasons, particularly in mid-latitude mountains [5,6]. In Europe, mountain areas are one of the most climate-sensitive and vulnerable regions [7]. They are critical habitats and natural water reservoirs and provide various ecosystem services and economic well-being. It should also be noticed that the majority of the annual runoff in European mountain areas is snowmelt-dominated [8]. It is challenging to predict snow cover changes in mountain areas at a regional scale, given their different responses to climate change in temperature and precipitation [5,9]. In these regards, in order to better understand regional responses and support adaptation strategies in the context of climate change, reliable information based on long-term time-series analysis of snowmelt processes during the ablation seasons is important for researchers, decision-makers, and stakeholders.

Earth Observation (EO) has a long history of application in snow monitoring. To date, different EO techniques (e.g., optical, radar, passive microwave, altimetry) have provided a timely, promising, and efficient approach to retrieve snow dynamics, including snowmelt processes [10]. Previous studies characterized snowmelt processes with several spatial parameters: SCA [11,12], snow line elevation (SLE) [13–15], or with temporal parameters: snowmelt onset (SMO) [3,16], snow cover duration (SCD) [17,18], and snow persistence (SP) [19,20]. Besides, to further capture the spatiotemporal dynamics of SCA throughout an ablation season, snow depletion curves (SDCs) are often utilized [21,22]. Moreover, SDCs can also be employed in calibrating hydrological models (e.g., snow runoff model, SRM) with regards to discharge forecasting [23,24]. However, it remains challenging to perform climate-change-related snow studies in complex terrains based on EO data, since long-term records (>30 years) in detailed spatial resolution (<100 m) are often required [25,26]. To this end, EO is facing a typical challenge regarding the trade-off between spatial and temporal resolution, since none of the prevalently employed optical EO archives, i.e., Landsat, MODIS (moderate resolution imaging spectroradiometer), Sentinel-2, or AVHRR (advanced very high resolution radiometer), could heretofore satisfy such requirements for snow dynamics monitoring in European mountains.

To date, Landsat has the longest uninterrupted operation history, whose access became free-of-charge since 2008 [27]. However, cloud obstruction and the near-two-week revisit time reduce the density of the Landsat time-series, and make it challenging to monitor the long-term snow dynamics in mountain areas solely using Landsat-based time-series. Firstly, cloud obstruction reduces the number of valid pixels in Landsat scenes. To reduce the influence of this issue, regional snow line elevation (RSLE) is introduced as an alternative to frequently-used SCA, since RSLE does not require fully cloud-free imagery. RSLE is calculated from a dynamic statistical quantile of elevation of snow/land pixels distribution [15]. Secondly, the near-two-week revisit time increases the uncertainty in snowmelt observation, given that snowmelt is highly temporal dynamic and RSLE variation is not always monotonous during an ablation season due to potential intermediate snowfall events. To deal with this problem, accumulated air-temperature (AT), instead of date, is linked to snow dynamics to generate modified snow depletion curves (MSDCs) [28]. It is because of the high likelihood that the relationship between AT and snow dynamic metrics (e.g., SCA) during an ablation season is monotonous. Ultimately, combining RSLE and MSDCs may provide a potential method to characterize long-term snowmelt processes during ablation seasons in mountain areas.

The overall objective of the present study is to derive 35-year regional snow line dynamics during the ablation seasons utilizing (semi-) high-resolution and free-of-charge optical dataset. For this purpose, a readily applicable framework has been developed. The framework takes advantage of the 30 m spatial resolution and more than three-decade observation history of the Landsat archive, which is also the main data source for the present study. Since the Landsat archive alone is limited by cloud obstruction, RSLE is used for deriving snow line information under partial cloud-covered scenes. To reduce the effects of near-two-week revisit time, the time domain is replaced by AT to generate regional snow line retreat curves (RSLRCs). Also, we combined Landsat observations with the images acquired by optical sensors with similar configuration (i.e., advanced spaceborne thermal emission and reflection radiometer, ASTER), to further densify the time-series. Finally, the obtained RSLRCs are then used to illustrate the timing of the ablation season and the speed of regional snow line retreat in relation to the air temperature.

2. Data and Study Areas

2.1. Satellite Data and Pre-Processing

In the present study, three different (semi-) high resolution and free-of-charge optical data (see Table 1) are employed, i.e., (1) Landsat thematic mapper (TM), enhanced thematic mapper plus (ETM+), operational land imager/thermal infrared sensor (OLI/TIRS) between 1984 and 2018; (2) ASTER between 2000 and 2007 (since the ASTER/SWIR sensor was defected in late April, 2008, details see:

https://asterweb.jpl.nasa.gov/swir-alert.asp); and (3) Sentinel-2A/2B multispectral instrument (MSI) between 2015 and 2018. The processing levels of employed Landsat, ASTER, and Sentinel-2 products are radiometrically calibrated and orthorectified (i.e., Landsat-L1TP, AST_L1T, and Sentinel-2-L1C). To obtain physically comparable surface reflectance datasets, atmospheric corrections were performed with ATCOR-3 [29] for each Landsat, ASTER, and Sentinel-2 scene. Topographic corrections were also integrated into ATCOR-3 by employing slope and elevation information from the ASTER Global Digital Elevation Model Version 2 (GDEM V2) [30]. In this study, Landsat and ASTER data are used for analyzing long-term snow dynamics, since they are of a longer operational time span than Sentinel-2. Whereas taking advantage of shorter revisit time of combining Sentinel 2A and 2B data, the Sentinel-2 acquisitions have been used as an independent dataset for cross-validating the Landsat/ASTER-based RSLRCs.

Table 1. Configurations of utilized bands of the selected earth observation (EO) sensors in this study: Landsat thematic mapper (TM), enhanced thematic mapper plus (ETM+), operational land imager/thermal infrared sensor (OLI/TIRS), advanced spaceborne thermal emission and reflection radiometer (ASTER), and Sentinel-2 (S2). CW stands for central wavelength in μm, and SR stands for spatial resolution in meters.

Sensor	Landsat						Sentinel-2			ASTER		
	TM/ETM+	CW	SR	OLI/TIRS	CW	SR	S2	CW	SR	ASTER	CW	SR
Green	2	0.56	30	3	0.56	30	3	0.56	10	1	0.56	15
Red	3	0.66	30	4	0.66	30	4	0.67	10	2	0.66	15
NIR	4	0.83	30	5	0.87	30	8a	0.83	20	3N	0.82	15
SWIR	5	1.65	30	6	1.61	3	11	1.61	20	4	1.65	30
TIRS	6	11.4	60/120	10	10.9	100				13	10.6	90

2.2. Auxiliary Data

For the purpose of accuracy assessment, the snow cover classifications are compared with the snow depth records from the National Oceanic and Atmospheric Administration - Global Historical Climatology Network (NOAA-GHCN, https://www.ncdc.noaa.gov/ghcnd-data-access, accessed on 06 March 2019) and the European Climate Assessment & Dataset (ECA&D, https://www.ecad.eu/dailydata/predefinedseries.php, accessed on 06 March 2019). Therein, the snow depth records between 1984 and 2018 originate from 65 meteorological stations within the selected study areas. Together with the validated snow cover classification, elevation information is indispensable to determine the RSLEs. The ASTER GDEM V2 [30] is hence employed to assess the statistical quantile of elevation of snow/land pixels distribution for RSLEs derivation. To generate RSLRCs, 2 m air-temperature reanalysis data between 1984 and 2018 are obtained from ERA-Interim [31]. Because glaciers influence snow line dynamics at a regional scale, it is required to calibrate RSLRCs in glaciated regions with the elevation information of the glacier(s). This elevation information is derived from the Randolph Glacier Inventory (RGI) and the ASTER GDEM.

2.3. Study Areas

Snowmelt processes are investigated in 11 montane catchments distributed across the mid-latitude European mountains (i.e., the Alps, the Carpathian Mountains, and the Pyrenees) during the ablation seasons (April to June) between 1984 and 2018. The numbers of analyzed Landsat, ASTER, and Sentinel-2 scenes for each catchment are listed in Figure 1. It should be noticed that the horizontal overlapping area of Landsat footprints is relatively large in mid-latitude regions, and the acquisition time difference between the two horizontally adjacent Landsat scenes thereof is nearly one week. If the major part of a catchment is within such an overlapping area, the data available in these catchments could be doubled. On the other hand, for large catchments that span over several horizontal overlapping footprints, it would be recommended to divide such catchments into sub-catchments. Otherwise, the mosaicked images from the Landsat scenes acquired in a one-week time difference may create artifacts in the retrieved snow dynamics.

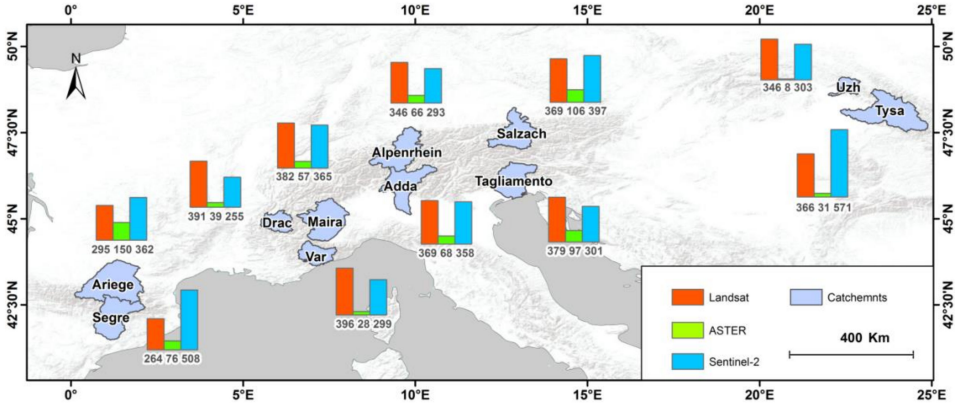

Figure 1. Overview of the study areas and number of available Landsat scenes from TM, ETM+, OLI/TIRS, ASTER and Sentinel-2 multispectral instrument (MSI) between April and June (1984–2018).

3. Methods

The methods can be categorized into four main steps: (1) pre-processing, (2) snow classification, (3) RSLE retrieval, and (4) RSLRC, as described in the corresponding subsections (Figure 2). In the first step, 8641 satellite images were pre-processed, including 3903 Landsat, 726 ASTER, and 4012 Sentinel-2 images. Thereafter, the reflectance of the images was normalized. The pre-processed images were then classified into four classes: snow, land, cloud, and water/shadow (Section 3.1). The classification results were subsequently validated against the meteorological station observations. Based on the validated classification results and the DEM, RSLEs were retrieved catchment-wisely according to the elevation distribution of the snow and land pixels (Section 3.2). Afterward, the accuracy assessment was performed based on two quality indices showing the percentage of valid pixels and erroneous pixels. In the last subsection, RSLRCs were calculated by linking sigmoid-transformed Landsat- and ASTER-derived RSLEs to the contemporary AT using linear regression. The results are cross-validated against the corresponding Sentinel-2-based RSLRCs.

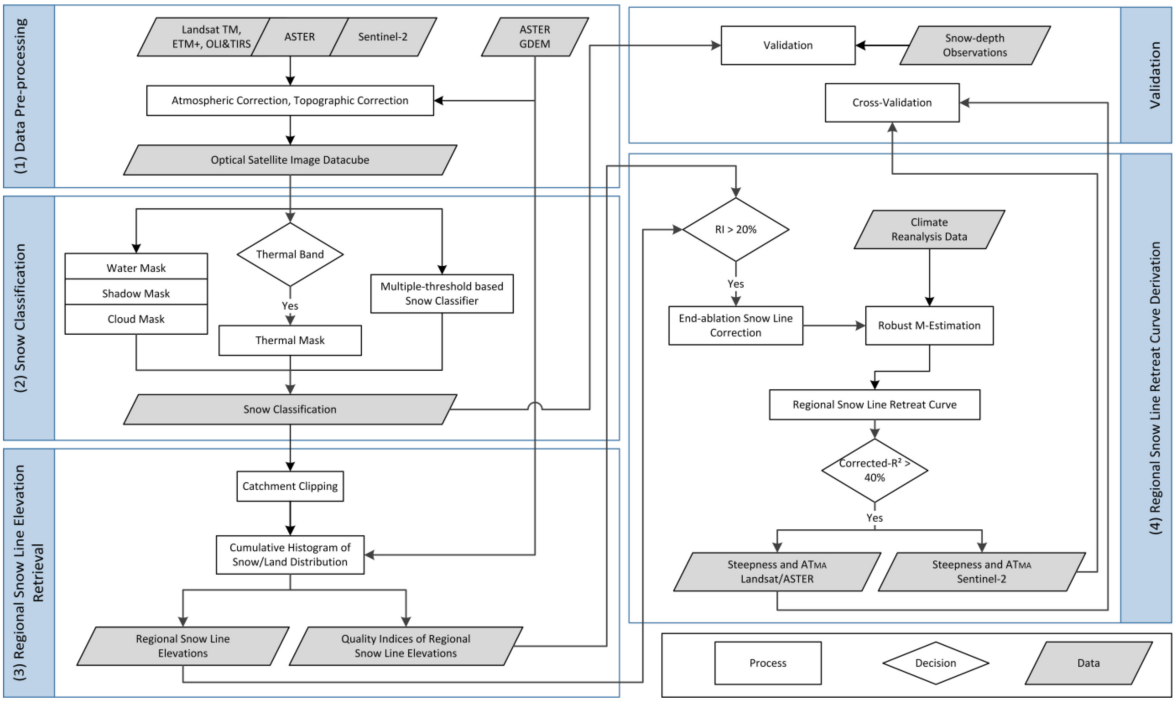

Figure 2. Overall workflow for: (1) pre-processing, (2) snow classification, (3) RSLE retrieval, and (4) RSLRC derivation.

3.1. Snow Cover Classification and Validation

To classify snow cover, there are two main processing parts, i.e., using a decision tree based on multiple thresholds to classify snow, and using masks (i.e., cloud mask, water mask, shadow mask and/or thermal mask) to exclude misclassifications:

- Snow classification: In this study, the algorithms developed by Klein et al. [32] and Poon and Valeo [33] is employed to classify snow. The algorithm is based on a decision tree with multiple thresholds on the normalized difference snow index (NDSI), the green band, and the near infra-red (NIR) band. To detect snow in forested areas, the NDSI-NDVI (normalized difference vegetation index) field is utilized to calibrate the snow cover classification results therein.
- Cloud mask: Three different types of cloud masks are applied because of different designations of Landsat, ASTER, and Sentinel-2. Firstly, the Mountainous Fmask (MFmask) [34–37] is deployed to mask out the clouds in Landsat scenes. Secondly, "s2cloudless" is employed to exclude the clouds in Sentinel-2 images, which is an automated single-scene pixel-based cloud detector developed by the Sentinel Hub's research team (available on GitHub: https://github.com/sentinel-hub/sentinel2-cloud-detector, accessed on 06 March 2019). Thirdly, the automatic cloud cover assessment (ACCA) [38,39] is applied to identify the clouds in ASTER scenes.
- Water mask: High NDSI values usually indicate the presence of the snow in optical EO imagery. However, such high NDSI values could also be observed in clear water bodies. Therefore, water bodies must be masked out to avoid misclassification. Because the water bodies commonly show positive normalized difference water index (NDWI) values, and the reflectance of water bodies in the green band is relatively low, the water mask is generated based on thresholding these two values.
- Shadow mask: Shadow-cast areas are normally treated as non-valid pixels. In this study, the shadow pixels are identified following the methods from the ESA satellite snow product intercomparison and evaluation exercise (SnowPEX) Team [40]. Thereafter, the shadow-cast pixels are masked out in the snow cover results.
- Thermal mask: Both Landsat and ASTER have thermal bands. To filter out bright and warm surfaces such as warm rocks in the classification results, a thermal threshold (<288 K) introduced by Metsämäki et al. [41] is applied to Landsat- and ASTER-based snow classifications. Sentinel-2 does not have any thermal band, which could potentially commit more commission errors over bright and warm targets.

The workflow chart is displayed in Figure 2, where snow classifier and masks are applied in sequence to obtain snow classification results. Thereafter, the binary snow classification results are validated using the contemporary NOAA-GHCN and ECA&D snow depth observations. The validation is based on the snow depth threshold proposed by Parajka et al. [42], i.e., if the observed snow depth is no less than 1 cm, the corresponding pixel is regarded as snow-covered, and vice versa.

3.2. Regional Snow Line Elevation Retrieval and Accuracy Assessment

The definition of the snow line elevation may vary according to objectives of the different applications (e.g., geographical studies, meteorological studies, hydrological studies) as discussed by Krajčí et al. [15]. In this study, we used the term RSLE proposed by Krajčí et al. [15] that is originally designed for remote sensing applications. RSLE is defined as the elevation where there are as few as possible snow pixels below it, and as few as possible land pixels above it. Methodologically, RSLE can be determined as the elevation where the minimum value of the sum of two cumulative histograms (i.e., cumulative histogram of snow pixels elevations and land pixels elevations) is reached (Figure 3).

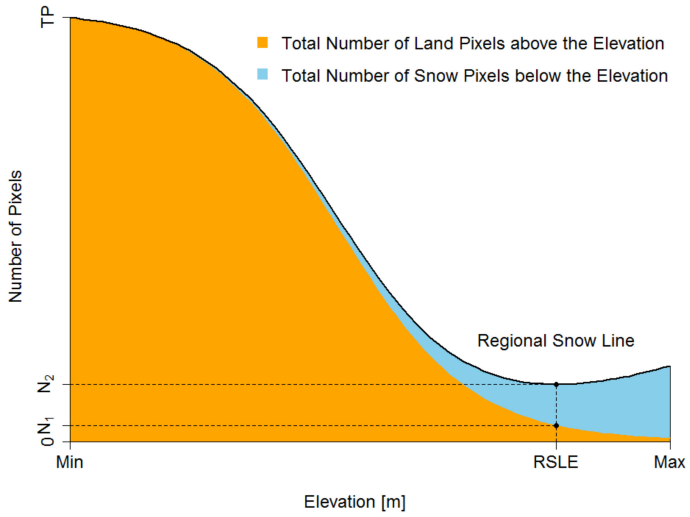

Figure 3. Estimation of regional snow line elevation (RSLE) from the combined cumulative histograms of the snow-covered pixels (in blue) and land pixels (in orange). In the *x*-axis, N_1 indicates that there are N_1 land pixels above the RSLE; (N_2-N_1) there are N_2 snow pixels below the RSLE, N_2 alone means the sum of land pixels above the RSLE and snow pixels below the RSLE, and TP stands for the total number of pixels.

To assess the accuracy of the retrieved RSLEs, two quality indices are introduced. The first quality index is representativeness index (RI) measuring the percentage of valid pixels (i.e., labeled as snow or land) within the spatial extent of a catchment. The calculation of RI is expressed as:

$$RI = \frac{F + S}{T_p} \quad (1)$$

where F and S are the number of snow-free and snow pixels within the catchment extent in classified images. T_p represents the total number of all the pixels (i.e., snow, land, cloud, water, and shadow) within the corresponding catchment extent. The optimal RI value is 100%, which indicates that there are no invalid pixels (i.e., cloud, shadow, water, missing value) within the catchment for RSLE retrieval. The second quality index, error index (EI), measuring the percentage of erroneous pixels (i.e., the number of the snow pixels below the RSLE, noted as S_b, and the number of snow-free pixels above the RSLE, noted as L_a) according to the corresponding RSLE. EI can be calculated as:

$$EI = \frac{S_b + L_a}{T_p} \quad (2)$$

By definition, the obtained RSLE should result in as few erroneous pixels as possible. EI is introduced as the ratio between the number of erroneous pixels and the total number of pixels (T_p), hence the best EI value is 0%.

3.3. Regional Snow Line Retreat Curve (RSLRC) Derivation and Validation

Once the RSLEs during each ablation season are retrieved, RSLRCs can be calculated, which describe the recession of the regional snow line over the ablation season. The RSLRC links the AT and RSLEs using the robust M-estimation [43]. The typical shape of a RSLRC is sigmoid, and therefore a logistic link function is firstly applied (Equation (3)). The robust regression is then implemented using the '*rlm*' library in R. The formulas of the RSLRC can be expressed by Equations (3)–(5):

$$RSLE_i = \frac{RSLE_{max}}{1 + e^{k \cdot AT_i + b}} \quad (3)$$

$$AT_{MA} = \frac{b}{-k} \tag{4}$$

$$AT_i = \int_0^i \left(\overline{T}_i - T_0\right) \cdot di + AT_0 \approx \sum_1^i \frac{\sum_{j=1}^4 \left(\overline{T}_{ij} - T_0\right) \times 6}{24} + AT_0 \tag{5}$$

where the $RSLE_{max}$ is the highest RSLE, which equals to the highest elevations from the DEM. In case of the glaciated areas, $RSLE_{max}$ is estimated by the 95th percentile of the elevations in delineated glacier outlines from the RGI. The slope (k) is always a negative value, whose absolute value represents the steepness of the RSLRC. The ratio between the intercept (b) and $-k$ (Equation (4)) is a coefficient indicating the AT of the mid-ablation season (AT_{MA}, the mid-point of the RSLRC). The generalized behavior of the RSLRC in relation to the coefficients is illustrated in Figure 4. AT_i represents the AT at the ith day within the ablation season, which is the integral of the daily temperature above the base temperature (T_0) added by the AT from the previous month (AT_0). This calibrates the shift of consecutive temperatures below 0 °C at the beginning of an ablation season. In this study, AT_i is approximated by the daily average of four 2 m air-temperature measures at a 6-h interval, and the base temperature is equal to the melting point 0 °C for snow/ice (Equation (5)).

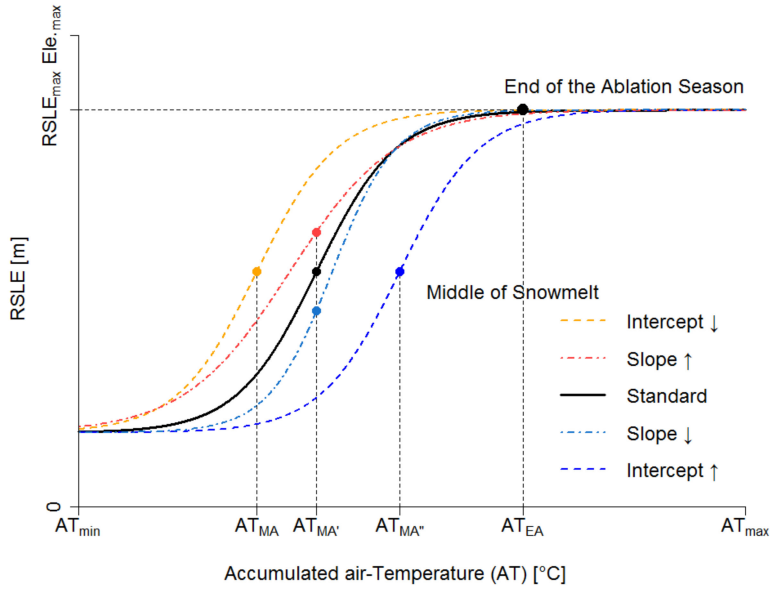

Figure 4. Theoretical regional snow line retreat curve (RSLRC) based on the accumulated air-temperature (AT) and RSLE. AT_{EA} is the AT at the end of the ablation season, whose RSLE is the $RSLE_{max}$. AT_{min} and AT_{max} are the minimum/maximum AT observed within the ablation season. AT_{MA} is the mid-point of the RSLRC, which is the AT of mid-ablation season. The solid line represents the standard situation, and the dash lines are the RSLRCs with different regression coefficients. The dash lines and dot-dash lines represent the behaviors of the RSLRCs in different slope and intercept values.

To guarantee the quality of the input RSLEs, a threshold of RI > 20% has been set to filter out RSLE results that may not be representative due to the lack of valid observations. Moreover, an end-ablation snow line correction is involved in the processing chain. It detects all input RSLEs within the maximum ± 10% of the elevation range in the catchments. If the number of end-ablation RSLEs is more than 80% of the total observation amount, then the RSLRCs would not be generated as too few observations of the regional snow line retreat are captured. If the number of end-ablation RSLEs is more than 50% of the total observation amount, only half of the RLSEs are included in the RSLRCs. This is because the breakdown point of the robust M-estimation is approximately 0.5, meaning more than 50% of end-ablation RSLEs would provide erroneous weights to the observations.

With regards to the accuracy assessment, the corrected coefficient of determination (corrected-R^2) for robust regression [44], mean absolute error (MAE) and root mean square error (RMSE) are calculated to evaluate the retrieved RSLRCs. To date, since the Sentinel-2 data only cover the ablation seasons 2016–2018, it does not bring a significant improvement to the 35-year time-series. On the other hand, given that the Sentinel-2 archive has the best data availability within its available years, Sentinel-2-derived RSLRCs constitute a valuable independent dataset to cross-validate the Landsat/ASTER-derived RSLRCs.

4. Results

The present study aims to characterize regional snow line dynamics during the ablation seasons. Within this context, two aspects of the regional snow line dynamics are presented in the following subsections, i.e., intra-annual and inter-annual variations of regional snow lines. Also, a comprehensive accuracy assessment is provided in the last subsection.

4.1. Intra-Annual Variations of Regional Snow Lines during the Ablation Season 2018

To demonstrate the intra-annual variations of the regional snow lines, RSLEs during the ablation season 2018 are displayed in Figure 5. The RSLEs are derived from the Landsat OLI/TIRS and ETM+ observations, representing the general situation when dual Landsat/ASTER sensors are in orbit. Given that the acquisition dates of Landsat images vary spatially, an ablation season is divided into nine categories (i.e., early/middle/end of April/May/June) in a 10-day time interval for better demonstration. Moreover, to better visualize the spatiotemporal distribution of the RSLEs, an overview of the Alpenrhein catchment is additionally illustrated in Figure 5. Spatially, in the northern Pyrenees (i.e., Ariege) RSLEs are lower than in the southern part (i.e., Serge). Besides, the regional snow line in the northern part of Pyrenees is preserved longer compared to the southern part. In the two Carpathian catchments, particularly in Uzh, the RSLEs last much shorter than in other investigated catchments during the ablation season 2018. In contrast, the regional snow lines are still preserved at the end of the ablation season 2018 in most of the Alpine catchments.

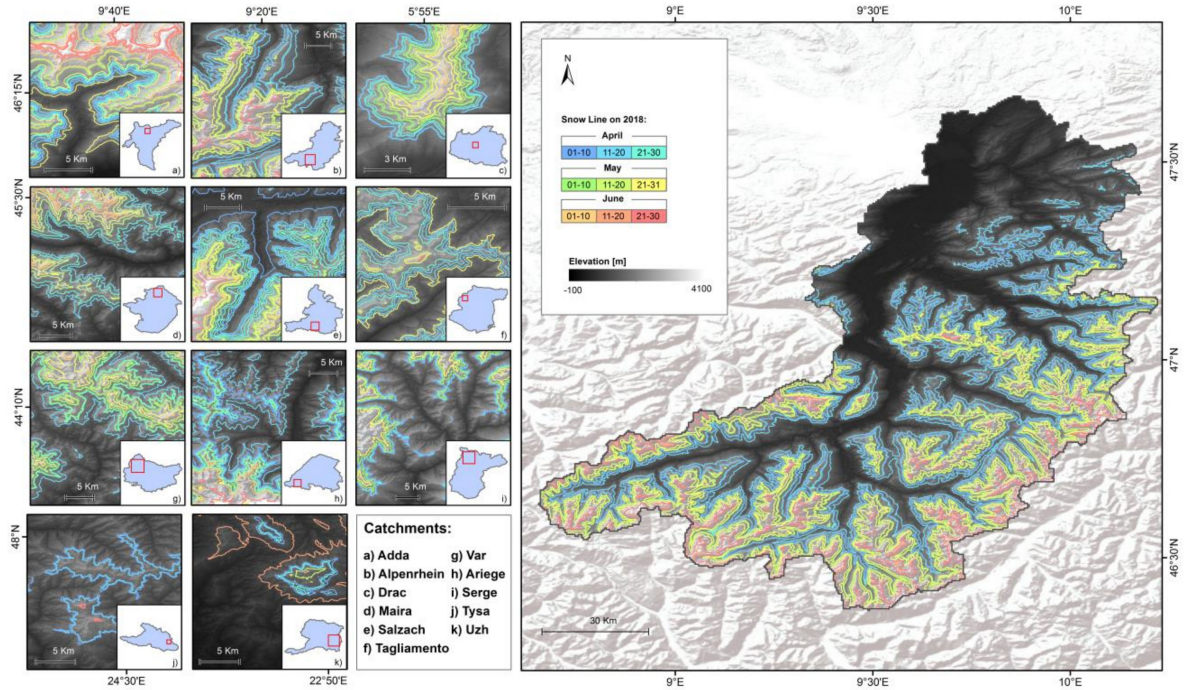

Figure 5. Snow lines based on RSLEs during the ablation season (April to June) 2018 within the investigated catchments: (**a**) Adda, (**b**) Alpenrhein, (**c**) Drac, (**d**) Maira, (**e**) Salzach, (**f**) Tagliamento, (**g**) Var, (**h**) Ariege, (**i**) Serge, (**j**) Tysa, and (**k**) Uzh. The right part is an overview of RSLEs in Alpenrhein.

Regarding the temporal pattern, the occurrence of the reddish color indicates the snow line at the end of the ablation season (i.e., the end of June), which should be located around the highest elevation. Otherwise, once the regional snow lines in reddish color are located in lower elevation zones compared with previous ones, it indicates the occurrence of an intermediate snowfall event. Therefore, these results could help identify anomalies, such as intermediate snowfall events observed in Figure 5, where reddish/yellowish regional snow lines are of lower elevation than bluish/greenish ones. For example, the yellow-colored (end of May) regional snow line appears in Adda and Tagliamento, and the coral-colored (end of June) regional snow line is observed within Uzh. In addition, within the Carpathian region, regional snow lines are rarely observed at the end of the ablation season.

4.2. Inter-Annual Variations of Regional Snow Lines during the Ablation Seasons 1984–2018

To demonstrate the inter-annual regional snow line variations, the time-series of the AT_{MA} and steepness from RSLRCs are shown in Figure 6 for each study area. In terms of the amount of the usable RSLRCs after the quality controls (Section 3.3), the Alpine catchments, as well as the northern Pyrenean catchments, are of the highest RSLRC quantity (29 years in average). Fewer RSLRCs are available for the catchments in the Carpathian Mountains and the southern Pyrenees (16 years on average). RSLRCs' scarcity appears mostly in the 1990s, particularly with the severest scarcity in the Carpathian Mountains. With such few RSLRC results, it is difficult to carry out statistically trustable analysis. Yet in most of the Alpine catchments and northern Pyrenean catchments, performing statistical analysis is still feasible.

The steepness of the RSLRC represents the velocity of regional snow line retreat because the AT is related to the day-of-year in the ablation season. Among the investigated catchments, only in Ariege (in the northern Pyrenees) a statistically significant (p-value = 0.036) negative trend of the RSLRCs' steepness has been observed, based on the 28-year observations. It indicates that the snow line is retreating significantly faster in this northern Pyrenean catchment. The 35-year AT time-series (see Figure 7) is indicating a tendency of increasing AT during the ablation seasons. It is thus also necessary to investigate the timing of the snow-clearance process. AT_{MA} illustrates how much AT is required for a regional snow line to reach the middle of the RSLE. Significant negative trends of AT_{MA} are detected in some Alpine catchments distant to the Mediterranean sea, i.e., Alpenrhein (p-value = 0.038) and Drac (p-value = 0.052). It indicates that lower than 3.77 and 3.99 Celsius per year are needed for the regional snow lines to reach the middle of the RSLRC in the Alpenrhein and Drac, respectively. As in these two catchments, no significant trend of RSLRCs' steepness is observed, it also suggests higher RSLEs in early April, and the disappearance of snow line retreat occurs earlier.

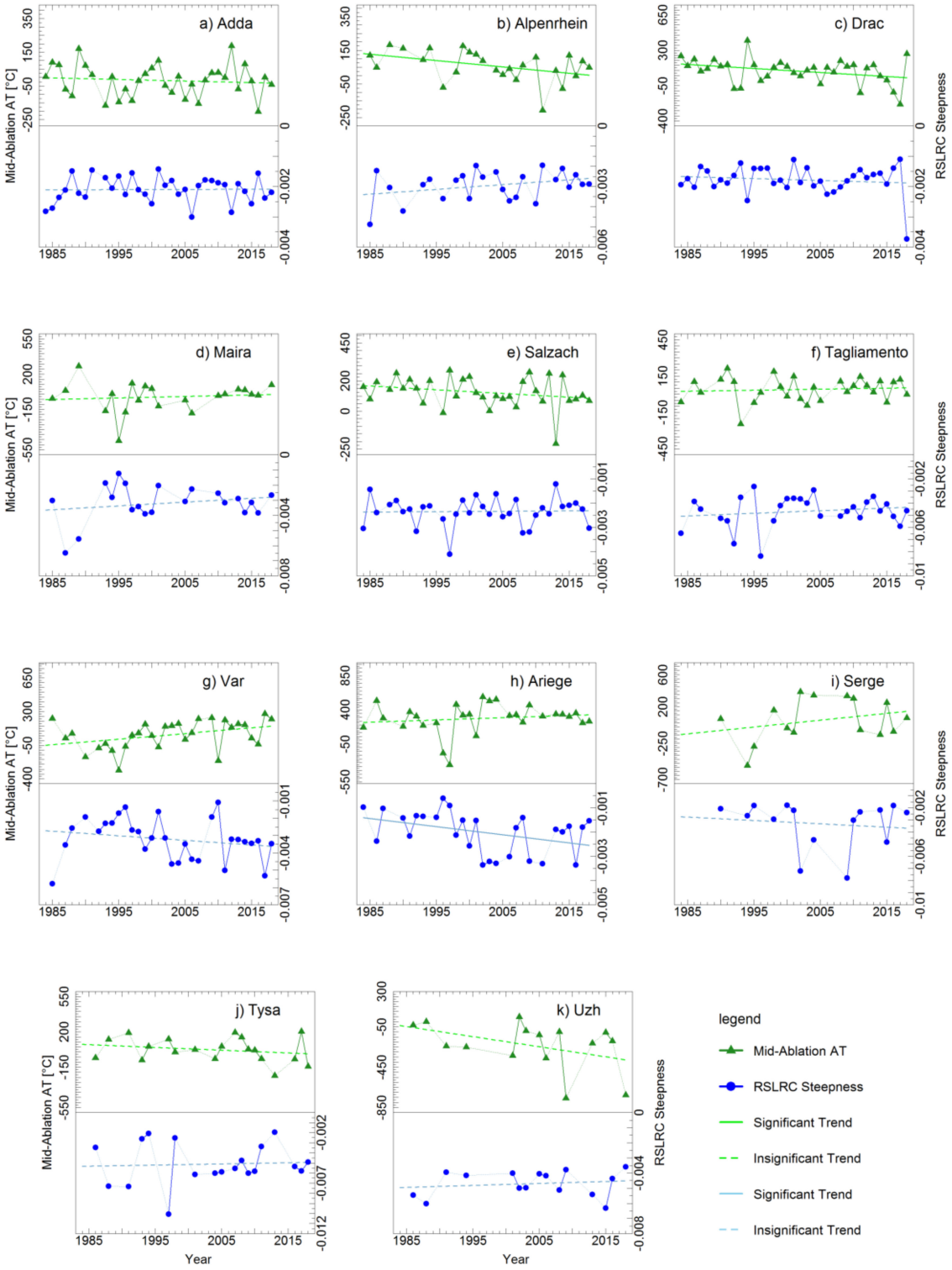

Figure 6. Steepness and accumulated air-temperature of the mid-ablation season (AT_{MA}) of the RSLRCs of the investigated catchments: (**a**) Adda, (**b**) Alpenrhein, (**c**) Drac, (**d**) Maira, (**e**) Salzach, (**f**) Tagliamento, (**g**) Var, (**h**) Ariege, (**i**) Serge, (**j**) Tysa, and (**k**) Uzh, between 1984 and 2018.

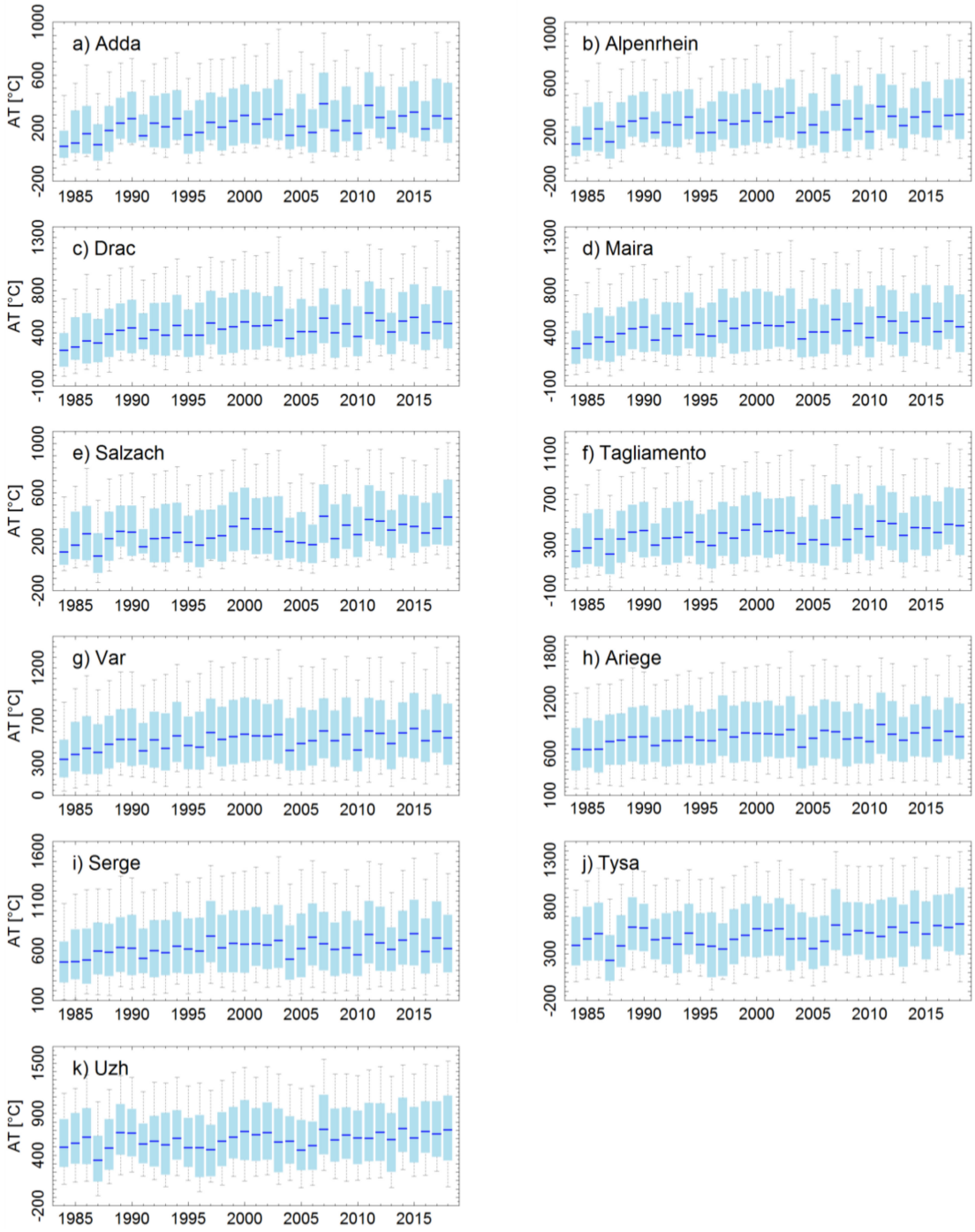

Figure 7. Box-whisker plots presenting max, min, median as well as 25th and 75th percentiles of the ATs between April and June of the investigated catchments (1984–2018): (**a**) Adda, (**b**) Alpenrhein, (**c**) Drac, (**d**) Maira, (**e**) Salzach, (**f**) Tagliamento, (**g**) Var, (**h**) Ariege, (**i**) Serge, (**j**) Tysa, and (**k**) Uzh, add by the AT in March for calibration purpose.

4.3. Accuracy Assessment

The uncertainties of the derived RSLRCs and the corresponding parameters are mainly caused and propagated by four sources: (1) misclassifications in the SCA maps, (2) errors of the employed DEM, (3) uncertainties of the RSLE results, and (4) imperfect model fit. Given that the accuracy of ASTER GDEM has been reported by several previous studies (e.g., [30,45,46]) and would stay systematic in the analyses, we only assess the three remaining error sources.

4.3.1. Accuracy Assessment of the Snow Classification Results

The overall accuracy (OA) of the SCA maps has been reported as 96.71% and the Kappa coefficient is 0.72, according to 7720 ECA&D and NOAA-GHCN snow depth observations. In addition, based on the confusion matrix (Table 2), precision and recall are calculated. Precision equals to 83.25%, indicating that 83.25% of the classified snow pixels are truly snow-covered. The recall is 65.41%, meaning that 65.41% of the snow-covered pixels have been detected. Regarding the accuracies of the SCA maps derived from the acquisitions from different sensors, the OAs are reported as 94.38% (ASTER), 97.08% (Landsat), and 95.22% (Sentinel-2).

Table 2. Confusion matrix relating satellite-derived snow classifications and ground snow-depth observations.

		Snow Depth Observations		
		Snow	**Snow-Free**	**User's Accuracy**
Classification	Snow	348	70	83.25%
	Snow-free	184	7118	97.48%
	Producer's Accuracy	65.41%	99.02%	OA = 96.71%

4.3.2. Accuracy Assessment of the Regional Snow Line Elevations (RSLEs)

The accuracy assessment is implemented by investigating two quality indices (i.e., RI and EI in Figure 8) introduced in Section 3.2. The median percentages of the valid pixels within each catchment are above 60%, and the upper and lower quantiles thereof are near 90% and 40%, respectively. From the boxplots of the EIs, in general, the obtained RSLEs are of low (<5%) erroneous pixels percentage, i.e., the snow pixels below the corresponding RSLE and the land pixels above the corresponding RSLE.

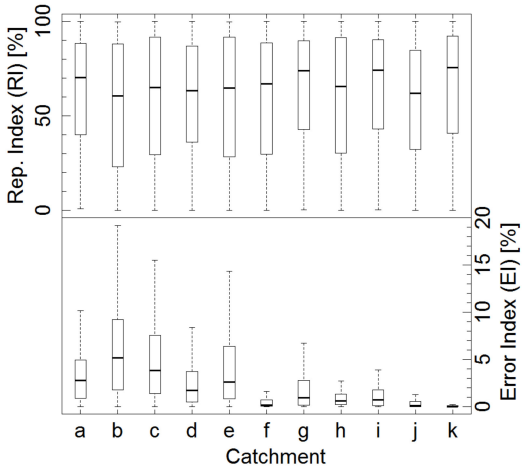

Figure 8. Accuracy assessment of the retrieved RSLE per catchment: Adda, Alpenrhein, Drac, Maira, Salzach, Tagliamento, Var, Ariege, Serge, Tysa, Uzh based on the representativeness index (RI) and error index (EI).

4.3.3. Accuracy Assessment of the Regional Snow Line Retreat Curves (RSLRCs)

To assess the performance of the robust M-estimation of the derived RSLRCs, the corrected-R^2 for robust estimation, MAE, and RMSE are calculated for each fitted RSLRC (Figure 9). The three metrics summarize the fit of the RSLRC to the RSLE inputs. Within the Alpine catchments (excluding Tagliamento), the median corrected-R^2 is around 0.90. Therein, more than 90% of the variance in the RSLEs can be explained by the variation of AT. According to the median, the RSLRCs explain approximately 10% less variation in the RSLEs in the Pyrenean catchments than the aforementioned Alpine catchments. In the Carpathian Mountains and Tagliamento, most of the RSLRCs are only

able to predict 65% of the RSLE variability according to their comparably small median corrected-R^2 (near 65%). Apart from Maira, the upper-quantile, median, and low-quantile of MAEs are generally below 30 m, 15 m, and 10 m, respectively. Most of the RMSEs are lower than 300 m. Maira is the catchment showing a comparably higher MAE and RMSEs than the other investigated catchments.

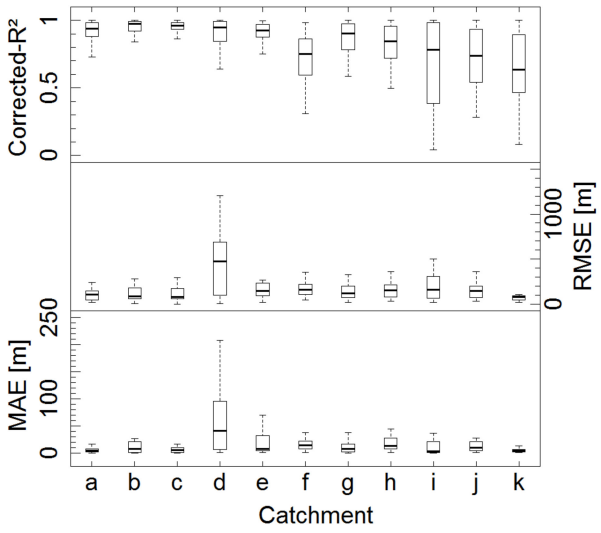

Figure 9. Accuracy assessment of the retrieved RSLRCs per catchment: Adda, Alpenrhein, Drac, Maira, Salzach, Tagliamento,Var, Ariege, Serge, Tysa, Uzh based on the corrected coefficient of determination (corrected-R^2), mean absolute error (MAE), and root mean square error (RMSE).

To cross-validate the RSLRC steepness and AT_{MA} obtained from the Landsat/ASTER-based RSLRCs in the past 35 years, Sentinel-2 data are employed to calculate the contemporary RSLRC steepness and AT_{MA} following the same workflow (Figure 2) between 2016 and 2018. The performance of each RSLRC using cross-validation is displayed in Figure 10. The cross-validation shows a high agreement between the RSLRCs calculated from Landsat/ASTER imagery and Sentinel-2 imagery. Regarding the bias of the estimated RSLRC steepness, Landsat/ASTER has an approximately 2.5% overestimation than the Sentinel-2. Yet near 3.5% underestimation is made by Landsat/ASTER-derived RSLRCs with regard to AT_{MA}. The coefficient of correlation (r) regarding the RSLRC steepness and AT_{MA} between Landsat/ASTER-based RSLRCs and Sentinel-2-based RSLRCs are 0.75 and 0.88, respectively, indicating a good agreement.

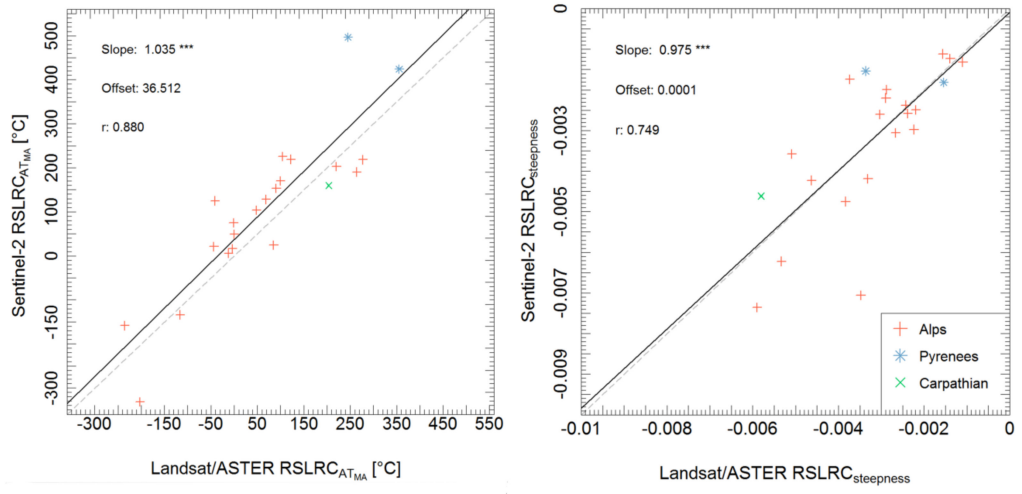

Figure 10. Comparison of estimated steepness of the RSLRCs and the AT_{MA} obtained from Landsat/ASTER imagery and Sentinel-2 imagery.

5. Discussion

In this section, we first discuss the challenges in accurately deriving RSLEs and RSLRCs with regards to data availability, data reliability, and method efficiency. Afterward, the limitations and difficulties concerning the validation data and validation scheme are summarized. Lastly, we discuss the observed regional snow line variations and the potential applications of our results.

5.1. Challenges in Accurately Deriving Regional Snow Line Elevations (RSLEs) and Regional Snow Line Retreat Curves (RSLRCs)

The uncertainties of the retrieved RSLEs mainly come from the accuracies of snow classifications and the involved DEM. The accuracies of snow classifications are affected by 1) cloud contamination, 2) signal saturation, 3) thermal-band absence, and 4) snow-in-forest detection. Among these factors, cloud contamination is the most influential. Commission errors are often recognized over bright targets including snow/ice [39,47,48] when applying the cloud masks (e.g., MFmask, ACCA). The misclassified pixels near the snow lines could potentially bias the statistics/distribution of the combined cumulative histograms of the snow and land pixels (Figure 3). Signal saturation (e.g., in Landsat 4/5 TM, Landsat 7 ETM+, ASTER [49,50]) could lead to poor accuracy in snow classification because the visible bands are often used to separate snow/cloud from other bright surfaces [51]. It is in line with the accuracy assessment results in Section 4.3.1. Moreover, it should be noticed that the thermal band is absent in Sentinel-2 data. It potentially leads to more commission errors when detecting snow in regions surrounded by warm bright land covers. Besides, detecting snow-in-forest using optical satellite data is challenging, since forest canopy covers up the snow beneath and casts shadow on its surroundings [32,52]. Obtaining accurate DEM in mountain areas are problematic for either interferometric method or photogrammetric method based on spaceborne satellite data. Often, the correlation algorithm for photogrammetric DEM generation fails over snow-covered areas [53,54], while an interferometric DEM has the problems of the voids in the original data [55]. In the present study, the errors induced by the employed DEM stay systematic, since they are largely counteracted. Given that airborne LiDAR can produce a DEM with high accuracy, further studies with regards to accuracy improvement should consider airborne LiDAR DEMs as valuable alternatives to interferometric or photogrammetric DEMs.

The accuracies of the derived RSLRCs depend on the availability and the representativeness of the input RLSE data, as well as the efficiency of the regression model. Data availability of spaceborne optical images varies spatiotemporally (especially in high mountain regions), due to cloud cover, acquisition plans (e.g., "commercialization era" [56]), sensor anomalies (e.g., Landsat 7 ETM+ SLC-off issue [57]) and footprint patterns [13]. Therein, cloud obstruction is the major issue, as clouds usually persist for a long time during the winter in European mountains. The resultant missing observations lead to the failure in RSLRC derivation, as shown in Figure 6. Moreover, footprint pattern is strongly influencing the data availability at a catchment scale. Taking Landsat as an example, the acquisition date difference of two horizontally adjacent footprints is often one week, thus data availability therein can be potentially doubled. In terms of the representativeness of the input data, apart from the accuracy of input RSLEs (Section 5.1), the accuracy of RSLRCs is also associated to the intermediate snowfall events, which create anomalously low RSLEs that are often treated as the 'outliers' in the RSLRCs. Since there is a high probability of intermediate snowfall events during accumulation seasons and the beginning of the ablation seasons, the present method is more suitable for middle-to-late ablation seasons. Furthermore, the heterogeneous geographical settings (e.g., aspects, solar irradiation, slopes, climate characteristics) are influential, as RSLEs are regional products. However, due to cloud cover, splitting a catchment into several sub-zones can result in insufficient cloud-free pixels for RSLE derivation, especially around the cloud-prone windward slopes. Regarding the representativeness of the climate reanalysis data, the original spatial resolution of the applied ERA-Interim is 80 km. It can potentially induce problems for catchments with a large proportion of plain areas (e.g., Maira catchment) because the obtained AT is, in fact, more representative for the snow-free areas. Such coarse resolution

also results in the omission of temperature variation in complex terrains. Further researches employing higher resolution climate reanalysis data, e.g., ERA-5 reanalysis dataset (32 km), COSMO-REA6 (6 km), COSMO-REA2 (2 km), are desirable. Noteworthily, these higher resolution climate reanalysis data are often only available for a limited time or spatial extent.

It must be noticed that the main objective of generating RSLRCs in the present study is not to predict intermediate RSLEs between two ATs (or two dates), but rather to characterize the regional snow line behavior during an ablation season. Therefore, the most crucial aspects of the regression models are breakdown point and goodness of model fit. Robust regression models (i.e., robust M-estimation) often have a higher breakdown point, meaning they could handle a larger amount of contaminated observations (e.g., RSLEs after an intermediate snowfall event) than conventional ordinary least squares (OLS) regression. Therefore, they can reduce the influences of high leverage outliers (e.g., intermediate snowfall events), and avoid biased-steepness from the logistic curve. In addition, to further alleviate the impacts of intermediate snowfall and temperature anomalies, the time-domain in RSLRCs is replaced by AT. To eliminate contaminated input data, RSLEs are filtered based on RI. To address the second concern (i.e., the goodness of model fit), a threshold of corrected-$R^2 > 0.4$ is chosen to exclude the RSLRCs that predict less than 40% of the variability of the regional snow line retreat. Section 4.3.3 further confirms that the involved RSLRCs are mostly of a corrected-$R^2 > 0.85$ in Alpine catchments, indicating a good fit of the applied regression models. Given that it is not appropriate to evaluate the model fit solely with the coefficient of determination, we have processed the Sentinel-2 time-series in the last three years to carry out a cross-validation to check the robustness of the RSLRCs. The high agreement between Sentinel-2-based and Landsat-based RSLRCs indicates that the method is valid for catchments where RSLRCs can be obtained under the abovementioned constraints.

5.2. Challenges of Validation

Validating long-term RSLEs and RSLRCs from (semi-) high-resolution optical satellite data is extremely challenging due to the lack of data and validation techniques. Conventionally, the validation of snow-related products can be realized using field measurements or satellite data of higher resolution. For instance, Krajčí et al. [15] combined the automatic weather station (AWS) with snowfield measurements to validate the MODIS-derived RSLE results. However, the elevation interval is 100 m and the study area is regional. For a larger spatial extent and finer resolution, a considerable amount of field measurements are required, which is unpractical due to intensive labor and material requirements and low accessibility in mountain areas. In addition, meteorological station data may not be dense enough to validate RSLEs results retrieved from (semi-) high-resolution data. Also, neither historical field measurements nor meteorological station data can reach back to 1980s. Regarding the satellite data with higher spatial resolution, the drawbacks are: (1) they are usually not free-of-charge; (2) they only have visible/near-infrared (Vis/NIR) or even only visible bands, leading to great difficulties to separate snow and other bright targets; (3) The swath is much smaller than a Landsat footprint; (4) The satellite often follows an acquisition request and the revisit-time is much longer than Landsat; (5) the operational time-span rarely reaches back to 1980s. More importantly, such data are often acquired by optical sensors, which would have relatively similar cloud obstruction at a catchment extent at the same time. Therefore, the uncertainties below the cloud can be hardly revealed by such dataset.

Unmanned aerial vehicle (UAV) imagery is a potential dataset to validate the RSLE and RSLRC results independent of cloud obscurations. UAVs are flexible to deploy in the aspects of mounted sensors (e.g., multispectral, hyperspectral, thermal, microwave, LiDAR), acquisition date, and operation periods. The spatial resolution of UAV images is often higher than those acquired by satellites. Therefore, UAV imagery holds a great potential to provide highly detailed information about the snow cover, especially for cloud-covered areas. Alternatively, WebCAM data have the advantages of (1) cloud cover independence, (2) low-cost, (3) very high observation interval, and (4) relatively long history in observing some mountain regions. Apart from a relatively high demand in pre-processing, it is

so far a unique potential dataset for validation. To homogenously produce such a WebCAM dataset, it requires a great collaboration among countries and institutes. Besides, spaceborne synthetic aperture radar (SAR) data can penetrate the cloud cover, thus revealing the snow cover condition under the clouds. Based on the current method [58–60], total snow cover areas could be derived from the SAR observation with an accuracy of up to 98.1%. However, due to the data access policy, it would be very costly to apply for these data for long-term research at a large spatial scale.

It should be noticed that the present work provides an exploratory framework to produce a long-term and (semi-) high-resolution-based snow line product with a fundamental validation process. We have noticed that the presented validation scheme is imperfect, but it is the maximum of what researchers can do using the free-accessible data. In this context, further studies in relation to the validation are urgently desirable.

5.3. Observed Regional Snow Lines Dynamics

In term of the intra-annual variations, the RLSEs between April and June illustrate the snow clearance in the studied catchments during the ablation season 2018. However, the number of retrieved RSLEs strongly depends on the elevation range and the number of valid pixels. In some catchments, the number of RSLE observations is limited, particularly in the Carpathian Mountains. Taking the Carpathian catchment Uzh as an example, its maximum elevation is around 1500 m while the elevations of the rest catchments range from 2200 m to 4100 m. The regional snow lines are seldom persevered after May in Uzh, due to such relatively low maximum elevation. Although it would be logical to switch the observation period towards mid-winter, the chance of intermediate snowfall events is high during that time, leading to very high uncertainty. Also, the high cloud persistence in mid-winter [13] would further decrease the data usability. Thus, for such catchment of lower elevation, the method is not well-suited. Meanwhile, as presented in Section 4.1, we have identified intermediate snowfall events in three catchments: Adda (end-of-May), Tagliamento (end-of-May), and Uzh (end-of June). To confirm these three observed snowfall events, we have checked the SCA conditions from global snow pack (GSP), a MODIS-based daily gap-filled SCA product [56], at a catchment scale. From GSP results, three snowfall events have been confirmed.

Inter-annual variations results indicate that there is a significant negative trend of the regional snow line retreat in the northern Pyrenean catchment Ariege. In the context of the increasing AT, it would result in a shortened ablation season, which is in line with the results from Buisan et al. [57]. On the other hand, temporal shifts of RSLRCs have been observed. Based on our linear trend analysis on AT_{MA}, there are significant negative trends in the Alpine catchment Alpenrhein and Drac. It indicates a tendency of a shortened ablation season, and higher RSLEs in April. The results are in line with previous studies [16,61,62]. Meanwhile, we discovered an obvious RSLRC scarcity in the Carpathian catchments compared to the other investigated catchments. It indicates that our method is not well-suited for deriving RSLRCs for the Carpathian Mountains, as the robust M-estimation failed to predict the majority of the regional snow line recession represented by the low corrected-R^2 values. There are two main reasons, i.e., insufficient valid RSLE inputs and intermediate snowfall events [13]. Besides, snow can be completely melted in the early months due to the low maximum elevation. The factors above make the RSLEs noisy and difficult to fit by a simple curve.

The presented results can be further used in applications with regards to snow cover phenology, climate change, winter tourism/sport, as well as flora and fauna. Snow cover phenology is a vital perspective of snow cover dynamics, which includes snow accumulation onset (SAO), snowmelt onset (SMO), snowmelt end (SME), snow cover duration, to name a few. However, given the revisit time and intermediate snowfall event occurrence, (semi-) high-resolution optical EO sensors like Landsat is rather for monitoring snow dynamics in middle-to-late ablation season. Since RSLEs indicate the spatial snow cover in the altitudinal direction, it could better illustrate the dynamics of snow clearance rather than the whole snowmelt process. This is because of the lower snowfall frequency and cloud coverage in the late ablation season. Furthermore, quantitate analyses linking RSLE dynamics

with other ECVs is beneficial to enhance the comprehension of regional response climate change. Thereby, better adaptation strategies could be made accordingly. Snowmelt run-off is vital to water management and disaster warning in snowmelt-dominant catchments. Run-off can be predicted by calibrating hydrological models using spatial snow coverage derived from the RSLRCs. It would be intriguing to compare the performance using (semi-) high-resolution-based snow information and medium-resolution-based information [63] in mountain areas. Winter tourism/sport management requires detailed spatial snow cover data for hiking routine planning, artificial snow planning, as well as the operation period length. Flora and fauna in high mid-latitude mountain regions are influenced by the snowline dynamics. The spatiotemporal snow dynamics affect the plant phenology [64–66], and animal activity [67–69].

6. Summary and Conclusions

This paper presents a readily applicable framework for retrieving regional snow line elevations (RSLEs) and their dynamics based on free-of-charge optical remote sensing and climate reanalysis datasets. Snow cover areas (SCAs) are firstly classified using a multi-threshold decision tree and corrected with cloud/shadow/water/thermal masks. The overall accuracy of the SCA results are around 96.71% according to 7720 meteorological snow-depth observations. The RSLEs are subsequently determined by the spatial distribution of the classified snow-covered and snow-free areas. The majority of the RSLEs are based on satellite images with more than 60% valid pixels (cloud-free and non-shadow) and are representative (>95% of the snow/land pixels) of the spatial distribution of snow in the altitudinal direction. Then the RSLEs are combined with accumulated air-temperatures (AT) to derive regional snow line retreat curves (RSLRCs) in a sigmoid shape. Based on the robust M-estimation, the RSLRC steepness and AT_{MA} (AT of mid-ablation season) are derived to characterize the regional snow line dynamics during the ablation seasons 1984–2018. The applied robust M-estimation models predict approximately 90% (Alps), 80% (Pyrenees), and 65% (Carpathian Mountains) of the regional snow line retreat variations during the ablation seasons 1984–2018, according to the corrected coefficients of determination. Finally, the Landsat-derived results are cross-validated against the Sentinel-2-derived RSLRCs (2016-2018). The cross-validation shows that the Landsat-derived RSLRC steepness and AT_{MA} have only 2.5% overestimation and 3.5% underestimation, respectively, indicating good agreement with those derived from Sentinel-2 ($r = 0.75$ for the RSLRC steepness, $r = 0.88$ for AT_{MA}).

This framework has been applied to 11 mid-latitude catchments in Europe. The results with regards to the intra-annual variation illustrate the recession of the regional snow line during the ablation season. The highest RSLRC quantity (29 years in average) is obtained in the investigated Alpine and northern Pyrenean catchments. The missing RSLRCs occur mostly in the 1990s, particularly in the Carpathian Mountains. Regarding the intra-annual variations, the results show that: (1) The Alpine catchments preserve regional snow lines longer than the other investigated catchments; (2) RSLEs are lower in the northern Pyrenees than in the southern part; (3) RSLEs last the shortest in the Carpathian catchments; and (4) intermediate snowfall events occurred in Adda and Tagliamento during the end of May 2018, and in Uzh during the end of June 2018. Meanwhile, significantly (p-value = 0.036) fastened snow line retreat is detected in the northern Pyrenean catchment Ariege. In the Alpine catchment Alpenrhein and Drac, there are statistically significant trends of the RSLRC shift towards lower AT, in the magnitude of $-3.77\ °C{\cdot}a^{-1}$ (Alpenrhein) and $-3.99\ °C{\cdot}a^{-1}$ (Drac).

The applicability of the presented framework is mainly constrained by data availability and intermediate snowfall events. The framework performs well in the Alpine catchments but problematically in the Carpathian catchments, where historical cloud-free Landsat data are scarce, and intermediate snowfall events occur frequently. The sparse observations and weak model performance also lead to difficulties in interpreting the statistical results. To address these problems, the next step would be to increase the number of EO data, and to involve climate reanalysis data with improved spatial resolution. The introduced RSLRCs are able to ingest snow classification results from other optical sensors, e.g., CBERS (China–Brazil Earth Resources Satellite program), SPOT

(Satellite Pour l'Observation de la Terre), IKONOS; and SAR (synthetic aperture radar) sensors, e.g., ERS (European remote sensing satellites), Envisat-ASAR, Sentinel-1. Therefore, further studies of ingesting such datasets could improve the data availability, and reduce the impacts of cloud obscuration. Also, SAR could provide additional information about the snow cover, e.g., snow wetness, snow depth, snow water equivalent [70,71]. Such information is beneficial for advancing the comprehension with regards to regional snow line dynamics during ablation seasons. Besides, to account for more detailed spatial temperature information, the ERA-5 reanalysis dataset (32 km), COSMO-REA6 (6 km) and COSMO-REA2 (2 km) could be explored. Last but not least, the validation scheme could be improved using UAV (Unmanned Aerial Vehicle) and WebCAM data.

Author Contributions: Z.H. performed the Landsat data analyses and wrote the majority of the manuscript. A.J.D. gave guidance in research design, critically discussed the manuscript and added to and revised the manuscript. C.K. suggested the research design, guided data analyses, and strengthened the paper through critical discussion and review.

Funding: This research received no external funding.

Acknowledgments: The authors would like to thank the China Scholarship Council for the financial support of this research. The authors would also like to thank the anonymous reviewers for their elaborated and helpful remarks as well as constructive criticism to improve the quality of the paper.

Conflicts of Interest: The authors declare no conflict of interest.

References

1. Derksen, C.; Brown, R. Spring snow cover extent reductions in the 2008–2012 period exceeding climate model projections. *Geophys. Res. Lett.* **2012**, *39*. [CrossRef]
2. Mudryk, L.R.; Kushner, P.J.; Derksen, C.; Thackeray, C. Snow cover response to temperature in observational and climate model ensembles. *Geophys. Res. Lett.* **2017**, *44*, 919–926. [CrossRef]
3. Metsämäki, S.; Böttcher, K.; Pulliainen, J.; Luojus, K.; Cohen, J.; Takala, M.; Mattila, O.-P.; Schwaizer, G.; Derksen, C.; Koponen, S. The accuracy of snow melt-off day derived from optical and microwave radiometer data—A study for Europe. *Remote Sens. Environ.* **2018**, *211*, 1–12. [CrossRef]
4. Hoegh-Guldberg, O.; Jacob, D.; Taylor, M.; Bindi, M.; Brown, S.; Camilloni, I.; Diedhiou, A.; Djalante, R.; Ebi, K.; Engelbrecht, F.; et al. Impacts of 1.5 °C global warming on natural and human systems. Available online: https://www.ipcc.ch/sr15/ (accessed on 16 April 2019).
5. IPCC. *Climate Change 2013: The Physical Science Basis: Working Group I Contribution to the Fifth Assessment Report of the Intergovernmental Panel on Climate Change*; Cambridge University Press: Cambridge, UK, 2013.
6. IPCC. *Climate Change 2014: Impacts, Adaptation, and Vulnerability-Part B: Regional Aspects-Contribution of Working Group II to the Fifth Assessment Report of the Intergovernmental Panel on Climate Change*; Cambridge University Press: Cambridge, UK, 2014.
7. EC White Paper-Adapting to Climate Change: Towards a European Framework for Action. Available online: https://ec.europa.eu/health/ph_threats/climate/docs/com_2009_147_en.pdf (accessed on 6 March 2019).
8. Barnett, T.P.; Adam, J.C.; Lettenmaier, D.P. Potential impacts of a warming climate on water availability in snow-dominated regions. *Nature* **2005**, *438*, 303–309. [CrossRef] [PubMed]
9. Jennings, K.S.; Winchell, T.S.; Livneh, B.; Molotch, N.P. Spatial variation of the rain—Snow temperature threshold across the Northern Hemisphere. *Nat. Commun.* **2018**, *9*, 1148. [CrossRef]
10. Hu, Z.; Kuenzer, C.; Dietz, A.J.; Dech, S. The Potential of Earth Observation for the Analysis of Cold Region Land Surface Dynamics in Europe—A Review. *Remote Sens.* **2017**, *9*, 1067. [CrossRef]
11. Tekeli, A.E.; Akyürek, Z.; Şorman, A.A.; Şensoy, A.; Şorman, A.Ü. Using MODIS snow cover maps in modeling snowmelt runoff process in the eastern part of Turkey. *Remote Sens. Environ.* **2005**, *97*, 216–230. [CrossRef]
12. Dietz, A.J.; Wohner, C.; Kuenzer, C. European snow cover characteristics between 2000 and 2011 derived from improved MODIS daily snow cover products. *Remote Sens.* **2012**, *4*, 2432–2454. [CrossRef]
13. Hu, Z.; Dietz, A.; Kuenzer, C. The potential of retrieving snow line dynamics from Landsat during the end of the ablation seasons between 1982 and 2017 in European mountains. *Int. J. Appl. Earth Obs. Geoinf.* **2019**, *78*, 138–148. [CrossRef]

14. Parajka, J.; Bezak, N.; Burkhart, J.; Hauksson, B.; Holko, L.; Hundecha, Y.; Jenicek, M.; Krajčí, P.; Mangini, W.; Molnar, P.; et al. MODIS snowline elevation changes during snowmelt runoff events in Europe. *J. Hydrol. Hydromech.* **2019**, *67*, 101–109. [CrossRef]
15. Krajčí, P.; Holko, L.; Perdigão, R.A.P.; Parajka, J. Estimation of regional snowline elevation (RSLE) from MODIS images for seasonally snow covered mountain basins. *J. Hydrol.* **2014**, *519*, 1769–1778. [CrossRef]
16. Takala, M.; Pulliainen, J.; Metsamaki, S.J.; Koskinen, J.T. Detection of snowmelt using spaceborne microwave radiometer data in Eurasia from 1979 to 2007. *IEEE Trans. Geosci. Remote Sens.* **2009**, *47*, 2996–3007. [CrossRef]
17. Klein, G.; Vitasse, Y.; Rixen, C.; Marty, C.; Rebetez, M. Shorter snow cover duration since 1970 in the Swiss Alps due to earlier snowmelt more than to later snow onset. *Clim. Change* **2016**, *139*, 637–649. [CrossRef]
18. Hüsler, F.; Jonas, T.; Riffler, M.; Musial, J.P. A satellite-based snow cover climatology (1985–2011) for the European Alps derived from AVHRR data. *Cryosphere* **2014**, *8*, 73. [CrossRef]
19. Macander, M.J.; Swingley, C.S.; Joly, K.; Raynolds, M.K. Landsat-based snow persistence map for northwest Alaska. *Remote Sens. Environ.* **2015**, *163*, 23–31. [CrossRef]
20. Wayand, N.E.; Marsh, C.B.; Shea, J.M.; Pomeroy, J.W. Globally scalable alpine snow metrics. *Remote Sens. Environ.* **2018**, *213*, 61–72. [CrossRef]
21. Leaf, C.F. Areal extent of snow cover in relation to streamflow in Central Colorado. In Proceedings of the International Hydrology Symposium, Fort Collins, CO, USA, 6–8 September 1967; Volume 1, pp. 157–164.
22. Hall, D. *Remote Sensing of Ice and Snow*; Springer Science & Business Media: London, UK, 2012.
23. Rango, A.; Martinec, J. Application of a snowmelt-runoff model using Landsat data. *Hydrol. Res.* **1979**, *10*, 225–238. [CrossRef]
24. Martinec, J. Snowmelt-runoff model for stream flow forecasts. *Hydrol. Res.* **1975**, *6*, 145–154. [CrossRef]
25. WMO. The Role of Climatological Normals in a Changing Climate. Available online: https://library.wmo.int/doc_num.php?explnum_id=4546 (accessed on 6 March 2019).
26. GCOS. The Global Observing System for Climate: Implementation Needs. Available online: https://unfccc.int/sites/default/files/gcos_ip_10oct2016.pdf (accessed on 6 March 2019).
27. Wulder, M.A.; Masek, J.G.; Cohen, W.B.; Loveland, T.R.; Woodcock, C.E. Opening the archive: How free data has enabled the science and monitoring promise of Landsat. *Remote Sens. Environ.* **2012**, *122*, 2–10. [CrossRef]
28. Rango, A.; Martinec, J. Snow accumulation derived from modified depletion curves of snow coverage. In Proceedings of the Exeter Symposium, Hydrological Aspects of Alpine and High Mountain Areas, Exeter, UK, 19–30 July 1982; Volume 138, pp. 83–89.
29. Richter, R.; Schläpfer, D. Atmospheric/topographic correction for satellite imagery: ATCOR-2/3 User Guide. *DLR IB* **2011**, *2011*, 501–565.
30. Tachikawa, T.; Hato, M.; Kaku, M.; Iwasaki, A. Characteristics of ASTER GDEM version 2. In Proceedings of the 2011 IEEE International Geoscience and Remote Sensing Symposium, Vancouver, BC, Canada, 24–29 July 2011.
31. Berrisford, P.; Dee, D.; Fielding, K.; Fuentes, M.; Kallberg, P.; Kobayashi, S.; Uppala, S. The ERA-interim archive. *ERA Rep. Ser.* **2009**, 1–16. Available online: https://www.ecmwf.int/file/21497/download?token=-Qu7p9eo (accessed on 16 April 2019).
32. Klein, A.G.; Hall, D.K.; Riggs, G.A. Improving snow cover mapping in forests through the use of a canopy reflectance model. *Hydrol. Process.* **1998**, *12*, 1723–1744. [CrossRef]
33. Poon, S.K.M.; Valeo, C. Investigation of the MODIS snow mapping algorithm during snowmelt in the northern boreal forest of Canada. *Can. J. Remote Sens.* **2006**, *32*, 254–267. [CrossRef]
34. Foga, S.; Scaramuzza, P.L.; Guo, S.; Zhu, Z.; Dilley, R.D.; Beckmann, T.; Schmidt, G.L.; Dwyer, J.L.; Hughes, M.J.; Laue, B. Cloud detection algorithm comparison and validation for operational Landsat data products. *Remote Sens. Environ.* **2017**, *194*, 379–390. [CrossRef]
35. Zhu, Z.; Woodcock, C.E. Object-based cloud and cloud shadow detection in Landsat imagery. *Remote Sens. Environ.* **2012**, *118*, 83–94. [CrossRef]
36. Zhu, Z.; Wang, S.; Woodcock, C.E. Improvement and expansion of the Fmask algorithm: Cloud, cloud shadow, and snow detection for Landsats 4-7, 8, and Sentinel 2 images. *Remote Sens. Environ.* **2015**, *159*, 269–277. [CrossRef]

37. Frantz, D.; Haß, E.; Uhl, A.; Stoffels, J.; Hill, J. Improvement of the Fmask algorithm for Sentinel-2 images: Separating clouds from bright surfaces based on parallax effects. *Remote Sens. Environ.* **2018**, *215*, 471–481. [CrossRef]
38. Irish, R.R.; Barker, J.L.; Goward, S.N.; Arvidson, T. Characterization of the Landsat-7 ETM+ automated cloud-cover assessment (ACCA) algorithm. *Photogramm. Eng. Remote Sens.* **2006**, *72*, 1179–1188. [CrossRef]
39. Irish, R.R. Landsat 7 automatic cloud cover assessment. In Proceedings of the Algorithms for Multispectral, Hyperspectral, and Ultraspectral Imagery VI, Orlando, FL, USA, 23 August 2000; Volume 4049, pp. 348–356.
40. Ripper, E.; Bippus, G.; Nagler, T.; Metsämäki, S.; Fernandes, R.; Crawford, C.J.; Painter, T.; Rittger, K. Guidelines for the Generation of Snow Extent Products from High Resolution Optical Sensors–FINAL. Available online: http://snowpex.enveo.at/Documents/D08_Guidelines_for_the_generation_of_snow_extent_products_from_HR_optical_sensors_FINAL_v1.0.pdf (accessed on 6 March 2019).
41. Metsämäki, S.; Pulliainen, J.; Salminen, M.; Luojus, K.; Wiesmann, A.; Solberg, R.; Böttcher, K.; Hiltunen, M.; Ripper, E. Introduction to GlobSnow Snow Extent products with considerations for accuracy assessment. *Remote Sens. Environ.* **2015**, *156*, 96–108. [CrossRef]
42. Parajka, J.; Pepe, M.; Rampini, A.; Rossi, S.; Blöschl, G. A regional snow-line method for estimating snow cover from MODIS during cloud cover. *J. Hydrol.* **2010**, *381*, 203–212. [CrossRef]
43. Hampel, F.R.; Ronchetti, E.M.; Rousseeuw, P.J.; Stahel, W.A. *Robust Statistics: The Approach Based on Influence Functions*; John Wiley & Sons: New York, NY, USA, 2011.
44. Willett, J.B.; Singer, J.D. Another cautionary note about R 2: Its use in weighted least-squares regression analysis. *Am. Stat.* **1988**, *42*, 236–238. [CrossRef]
45. Hirt, C.; Filmer, M.S.; Featherstone, W.E. Comparison and validation of the recent freely available ASTER-GDEM ver1, SRTM ver4. 1 and GEODATA DEM-9S ver3 digital elevation models over Australia. *Aust. J. Earth Sci.* **2010**, *57*, 337–347. [CrossRef]
46. Reuter, H.I.; Neison, A.; Strobl, P.; Mehl, W.; Jarvis, A. A first assessment of ASTER GDEM tiles for absolute accuracy, relative accuracy and terrain parameters. In Proceedings of the 2009 IEEE International Geoscience and Remote Sensing Symposium, Cape Town, South Africa, 12–17 July 2009.
47. Selkowitz, D.J.; Forster, R.R. An automated approach for mapping persistent ice and snow cover over high latitude regions. *Remote Sens.* **2016**, *8*, 16. [CrossRef]
48. Hagolle, O.; Huc, M.; Pascual, D.V.; Dedieu, G. A multi-temporal method for cloud detection, applied to FORMOSAT-2, VENμS, LANDSAT and SENTINEL-2 images. *Remote Sens. Environ.* **2010**, *114*, 1747–1755. [CrossRef]
49. Dozier, J. Snow reflectance from Landsat-4 thematic mapper. *IEEE Trans. Geosci. Remote Sens.* **1984**, 323–328. [CrossRef]
50. Dozier, J. Spectral signature of alpine snow cover from the Landsat Thematic Mapper. *Remote Sens. Environ.* **1989**, *28*, 9–22. [CrossRef]
51. Zhu, Z.; Woodcock, C.E. Continuous change detection and classification of land cover using all available Landsat data. *Remote Sens. Environ.* **2014**, *144*, 152–171. [CrossRef]
52. Maurer, E.P.; Rhoads, J.D.; Dubayah, R.O.; Lettenmaier, D.P. Evaluation of the snow-covered area data product from MODIS. *Hydrol. Process.* **2003**, *17*, 59–71. [CrossRef]
53. Kääb, A. Monitoring high-mountain terrain deformation from repeated air-and spaceborne optical data: examples using digital aerial imagery and ASTER data. *ISPRS J. Photogramm. Remote Sens.* **2002**, *57*, 39–52. [CrossRef]
54. Svoboda, F.; Paul, F. A new glacier inventory on southern Baffin Island, Canada, from ASTER data: I. Applied methods, challenges and solutions. *Ann. Glaciol.* **2009**, *50*, 11–21. [CrossRef]
55. Frey, H.; Paul, F. On the suitability of the SRTM DEM and ASTER GDEM for the compilation of topographic parameters in glacier inventories. *Int. J. Appl. Earth Obs. Geoinf.* **2012**, *18*, 480–490. [CrossRef]
56. Dietz, A.J.; Kuenzer, C.; Dech, S. Global SnowPack: a new set of snow cover parameters for studying status and dynamics of the planetary snow cover extent. *Remote Sens. Lett.* **2015**, *6*, 844–853. [CrossRef]
57. Buisan, S.T.; Saz, M.A.; López-Moreno, J.I. Spatial and temporal variability of winter snow and precipitation days in the western and central Spanish Pyrenees. *Int. J. Climatol.* **2015**, *35*, 259–274. [CrossRef]
58. Muhuri, A.; Manickam, S.; Bhattacharya, A. Scattering mechanism based snow cover mapping using RADARSAT-2 C-Band polarimetric SAR data. *IEEE J. Sel. Top. Appl. Earth Obs. Remote Sens.* **2017**, *10*, 3213–3224. [CrossRef]

59. Nijhawan, R.; Das, J.; Raman, B. A hybrid of deep learning and hand-crafted features based approach for snow cover mapping. *Int. J. Remote Sens.* **2019**, *40*, 759–773. [CrossRef]
60. Wang, Y.; Wang, L.; Li, H.; Yang, Y.; Yang, T. Assessment of snow status changes using L-HH temporal-coherence components at Mt. Dagu, China. *Remote Sens.* **2015**, *7*, 11602–11620. [CrossRef]
61. Bulygina, O.N.; Razuvaev, V.N.; Korshunova, N.N. Changes in snow cover over Northern Eurasia in the last few decades. *Environ. Res. Lett.* **2009**, *4*, 45026. [CrossRef]
62. Tedesco, M.; Brodzik, M.; Armstrong, R.; Savoie, M.; Ramage, J. Pan arctic terrestrial snowmelt trends (1979–2008) from spaceborne passive microwave data and correlation with the Arctic Oscillation. *Geophys. Res. Lett.* **2009**, *36*. [CrossRef]
63. Déry, S.J.; Brown, R.D. Recent Northern Hemisphere snow cover extent trends and implications for the snow-albedo feedback. *Geophys. Res. Lett.* **2007**, *34*. [CrossRef]
64. Böttcher, K.; Aurela, M.; Kervinen, M.; Markkanen, T.; Mattila, O.P.; Kolari, P.; Metsämäki, S.; Aalto, T.; Arslan, A.N.; Pulliainen, J. MODIS time-series-derived indicators for the beginning of the growing season in boreal coniferous forest—A comparison with CO_2 flux measurements and phenological observations in Finland. *Remote Sens. Environ.* **2014**, *140*, 625–638. [CrossRef]
65. Thum, T.; Aalto, T.; Laurila, T.; Aurela, M.; Hatakka, J.; Lindroth, A.; Vesala, T. Spring initiation and autumn cessation of boreal coniferous forest CO_2 exchange assessed by meteorological and biological variables. *Tellus B Chem. Phys. Meteorol.* **2009**, *61*, 701–717. [CrossRef]
66. Asam, S.; Callegari, M.; Matiu, M.; Fiore, G.; De Gregorio, L.; Jacob, A.; Menzel, A.; Zebisch, M.; Notarnicola, C. Relationship between Spatiotemporal Variations of Climate, Snow Cover and Plant Phenology over the Alps—An Earth Observation-Based Analysis. *Remote Sens.* **2018**, *10*, 1757. [CrossRef]
67. Pöyry, J.; Böttcher, K.; Fronzek, S.; Gobron, N.; Leinonen, R.; Metsämäki, S.; Virkkala, R. Predictive power of remote sensing versus temperature-derived variables in modelling phenology of herbivorous insects. *Remote Sens. Ecol. Conserv.* **2018**, *4*, 113–126. [CrossRef]
68. Mills, L.S.; Bragina, E.V.; Kumar, A.V.; Zimova, M.; Lafferty, D.J.R.; Feltner, J.; Davis, B.M.; Hackländer, K.; Alves, P.C.; Good, J.M.; et al. Winter color polymorphisms identify global hot spots for evolutionary rescue from climate change. *Science* **2018**, *359*, 1033–1036. [CrossRef] [PubMed]
69. Zimova, M.; Hackländer, K.; Good, J.M.; Melo-Ferreira, J.; Alves, P.C.; Mills, L.S. Function and underlying mechanisms of seasonal colour moulting in mammals and birds: What keeps them changing in a warming world? *Biol. Rev.* **2018**, *93*, 1478–1498. [CrossRef] [PubMed]
70. Nagler, T.; Rott, H. Retrieval of wet snow by means of multitemporal SAR data. *IEEE Trans. Geosci. Remote Sens.* **2000**, *38*, 754–765. [CrossRef]
71. Pettinato, S.; Santi, E.; Brogioni, M.; Paloscia, S.; Palchetti, E.; Xiong, C. The potential of COSMO-SkyMed SAR images in monitoring snow cover characteristics. *IEEE Geosci. Remote Sens. Lett.* **2013**, *10*, 9–13. [CrossRef]